Anatomy of a Flash Flood in a Hyperarid Environment: From Atmospheric Masses to Sediment Dispersal in the Sea

Akos **Kalman**[a,b,c], Timor **Katz**[b], Miklos **Vincze**[e], Jake **Longenecker**[c], Alysse **Mathalon**[d], Paul **Hill**[d], Beverly **Goodman-Tchernov**[a]

[a] *University of Haifa, Department of Marine Geosciences, Leon Charney School of Marine Sciences, Mt. Carmel, Haifa 31905, Israel*

[b] *Israel Oceanographic and Limnological Research, P.O.B 8030, Haifa 31080, Israel*

[c] *University of Miami, Rosenstiel School of Marine, Atmospheric, and Earth Science, 4600, Rickenbacker Causeway, Key Biscayne, 33149, FL, USA*

[d] *Dalhousie University, Oceanography Department, 1355 Oxford Street, P.O.B 15000, Halifax, Nova Scotia B3H4R2, Canada*

[e] *HUN-REN Institute of Earth Physics and Space Science, Sopron, H-9400, Hungary*

Correspondence to: A. Kalman (~~axk2119@earth.miami.edu~~akoss.kalman@gmail.com)

Highlights

1. A hyperarid desert flash flood is described and documented *in situ* from its meteorological development to arriving into the offshore

2. Flood triggered by weak polar vortex, amplified Rossby wave, causing intense rainfall in Eilat

3. Flood discharged 25,000 tons of sediment within freshwater outflow, altering salinity and sediment concentrations in the sea

4. Sediment dispersal outflow alternated between hypopycnal and hyperpycnal flows due to shifting flood dynamics and related sediment concentrations

Keywords

flood dynamics, hyperpycnal flow, amplified Rossby wave, sedimentary record, Red Sea

Abstract

Flash floods in rivers near hyper-arid coastlines impact both land and marine environments, from recharging groundwater and supporting desert ecosystems to affecting marine water quality, organisms, and substrates. Few studies, however, have followed these events from atmospheric origins to marine effects. This study tracked a desert flash flood in October 2016 in Eilat, capturing stages from atmospheric conditions to sediment distribution at sea. Observations included satellite data, meteorological reports, floodwater discharge, and sediment levels from the Kinnet Canal outlet, alongside offshore turbidity and salinity data. Our findings indicate that a weakened polar vortex amplified a Rossby wave, triggering convective instability over the Eastern Mediterranean and northern Red Sea. In Eilat (mean annual rainfall = 27 mm, SD = 21 mm), 128% of the average annual rainfall occurred fell within hours, with the flood reaching the sea approximately 50 hours later and lasting 27 hours. Around 25,000 tons of sediment were discharged, causing offshore salinity drops (up to 1.75‰ below the seawater background) and fluctuations of suspended sediment concentrations due to varying flow rates. In turn, particle dispersal in the sea switched several times between hypopycnal (surface) and hyperpycnal (bottom) flows. These findings link the different stages of the flood and their cascading effects from air masses to sedimentary processes in the sea.

1   Introduction

1.1   Background

A large portion of continental shelf sediments in the shallow offshore originate from terrestrial sources delivered through rivers (Syvitski et al., 2005). In higher precipitation regions it arrives primarily through large perennial rivers, while in drier climates, such as deserts, fluvial sediments are often delivered via ephemeral rivers during sporadic precipitation events that may produce flash floods (Cohen and Laronne, 2005a).

Flash flood events are crucial for both sustaining desert terrestrial ecosystems (Gee and Hillel, 1988; Hereford et al., 2006) and enriching marine systems with essential nutrients and sediments, thereby altering the physical, chemical, and biological dynamics of coastal shelf ecosystems (Hickey et al., 2010). Rainfall in desert regions is typically short-lived, sometimes robust, spatiotemporally sporadic, and capable of evolving into flashfloods (Sharon, 1972). From a human perspective, these floods may cause property damage, loss of life, and disruptions to transportation and other infrastructure (Haggag and El-Badry, 2013). For instance, between 1900 and 2016, 39 severe floods in the Middle East – spanning Egypt, Israel, Jordan and Saudi Arabia – caused over 1500 fatalities and directly impacted around 300,000 people (de Vries et al., 2018).

Historically, cities along hyperarid coastlines were rare, but this has changed dramatically in recent decades (Neumann et al., 2015). Technological advancements, including desalination plants, air-conditioned buildings, and refrigerated freight containers, have facilitated the growth of cities worldwide in these less habitable locations (Barragán and de Andrés, 2015; Holdren and Ehrlich, 1974; Small and Nicholls, 2003). However, despite these advances, flood risk due to their relative rarity and unpredictability, remains an issue.

Flood forecasts generally rely on predictions of heavy precipitation, yet in hyperarid areas, rainfall is highly variable. This variability complicates the ability to predict whether the accumulation of runoff from different adjacent catchments will lead to coastal flashfloods, thereby posing challenges for early warnings and preparations in low-lying coastal cities (Cools et al., 2012). Understanding the specific processes and conditions that lead to, or do not lead to, flashflood and related fluvial sediment discharge is essential for improving forecast accuracy and flood preparedness.

Principally, in arid coastlines, the deposition of fluvial sediment into the sea represents the culmination of a series of interconnected events. These stages can be summarized as follows: 1) atmospheric conditions leading to precipitation, 2) the occurrence of precipitation, 3) the drainage of water through the watershed, 4) the formation of flash floods, 5) the transportation of water and sediments to the coastline, 6) the discharge of these elements from the coastal outlet into the sea, and 7) the subsequent dispersal and deposition within the marine environment (Cohen and Laronne, 2005b; Kalman et al., 2020a, 2022; Katz et al., 2015a; Mathalon et al., 2019; Mulder et al., 2003; Reid and Frostick, 1987). While aspects of these stages have been the subject of research (Allison et al., 2012; Blum and Törnqvist, 2000; Merz et al., 2021; Mullenbach and Nittrouer, 2000), comprehensive studies tracing the entire sequence for a specific event are lacking. Developing a framework that traces the entire sequence of events during a single flood can serve as a model for understanding similar processes in other arid coastal systems, even when only partial or less detailed data are available. Such a methodology could enhance our broader understanding of sediment dynamics and support environmental management, ecological conservation, urban planning in coastal deserts, and natural hazard assessment. Gaining such comprehensive insights would enhance our understanding of this ecologically vital system and could offer tangible benefits for environmental management, ecological conservation, urban development in coastal desert regions, and the assessment of natural hazards.

The aims of this study were 1) to capture the full sequence of a desert flood from meteorological precursors to eventual sediment discharge from an ephemeral coastal river and its dispersal in the sea; 2) to assess the dependence or relationship between parts of the sequence and their outcomes, and 3) to track and identify specific atmospheric antecedent conditions that contributed to the triggering mechanism of the flash flood.

To achieve these aims, we integrated records from regional meteorological data with in-situ environmental measurements of salinity, turbidity, temperature, and surficial water velocity preceding and during a flash flood event that discharged into the northern Red Sea / southern Negev Desert of Israel.

1.2   Previous Atmospheric and Precipitation studies

For decades, there has long been an interest in the linkages between meteorological conditions and resulting floods (El-Fandy, 1948). One of the earliest studies on meteorological trends and flooding was conducted by Ashbel (1938), who described several extreme precipitation and flooding events in Rutbah, Damascus, the Dead Sea and the Sinai Peninsula. The events occurred with the northward propagation of the Red Sea Trough, and descending cold air from the north.

At present, based on nearly 70 years of data reanalysis, the RST is 96% originated from Sudan (Almazroui et al., 2016), and is known to be the most active during the autumn and winter (Alpert et al., 2004a; Saaroni et al., 2020). Also, it is usually accompanied by upper-level westerlies or by an anticyclonic flow (Tsvieli and Zangvil, 2005); but under these conditions the RST is a dry system with no rain. Southeasterly winds blow the air over the sandy basins of Saudi Arabia, Iraq, and Syria, a process that often triggers aeolian transport of sediment towards the Eastern Mediterranean (Dayan et al., 2008). However, no single synoptic feature is solely responsible for the development of heavy rainfall over the Levant.

Kahana et al. (2002) labeled a thunderstorm producing RST as an 'Active RST' (ARST). Krichak and Alpert (1998) outlined a sequence that leads to the formation of these storms: moisture transport from equatorial Africa (1), followed by convection (2), and intensification of The Subtropical Jet Stream (3) thus enhancing RST expansion (4) and related moisture (5) towards the Levant. A detailed analysis of a severe October 1997 ARST event by Dayan et al., (2001) confirmed stages (2), (3) and (5). Other studies (Dayan et al., 2001, 2021; Kahana et al., 2002; De Vries et al., 2013; Ziv et al., 2005) emphasize the significant role of mid-latitude upper-level troughs in amplifying instability and driving rainfall.

Ziv et al. (2022) identified climatological precursors for cyclogenesis associated with the RST extending toward the Levant. Using automated cyclone tracking (Hochman et al., 2020; Ziv et al., 2015) from 1979 to 2017, they identified four patterns of upper-level trough approaching the Eastern Mediterranean: 1) a cyclone crossing the Levant from the southwest, 2) a trough from the northeast, 3) a trough from the west, and 4) scenarios without upper-level support. Notably, in the second category, intense rainfalls occured, driven by cold advection resembling a polar intrusion, which greatly increases static instability over the Levant.

1.3 Runoff and flood development in the hyperarid GAE

Short-lived, but intense rainfall sometimes occurs over the terrestrial drainage in the hyperarid landscape surrounding the Gulf of Aqaba-Eilat (GAE). Within hours, this water runoff may accumulate in the otherwise dry riverbeds (wadis), and if the water volume that accumulates is large enough, it can produce a flashflood. Lack of vegetation and poor soil development with low permeability (Cohen & Laronne, 2005 and references therein) also contributes to the prompt development of floods. The time between rainfall and initiation of the flooding depends on storm intensity, duration, catchment size and which part of the catchment receives the rain. Because of the temporally sporadic nature of the rain events, sometimes years can pass between consecutive events in the same drainage system. These extended non-flood periods allow for surface weathering processes to dominate (and dust to settle), leaving ample sediment available when rains do arrive (Cohen and Laronne, 2005a). Therefore, the emerging floods have high concentrations of suspended sediment that may even increase towards the terminal basins owing to transmission loss (Shentsis et al., 2001).

A sequence of instrument gauge stations was first installed in the southern Arava desert in 1966, set along ephemeral streams such as Nahal Yael (2 km long, 0.6 km^2 catchment area) that lead into larger tributaries (Schick and Lekach, 1993). These gauges have provided information regarding flow and sediment loads, demonstrating that sediment discharge is inconsistent. For example, during 33 years of monitoring, 14 years lacked any flow, and 8 years had flood events during which the flow terminated prior to the gauge at the lowest elevation (Clapp et al., 2000). The measured floods that terminated before reaching the sea delivered large amounts of sediment to the wadi system (100 tons of eroded sediment per km^2 per year (Schick and Lekach, 1993), 460 tons of sediment in a single event (Clapp et al., 2000)). ~~The total suspended solids (TSS) i~~In this local hyperarid wadi, total suspended solids (TSS) during ~~when~~ flooding ~~was~~ were measured at 44 grams per liter~~. from an~~based on an average ~~of~~ from ~~3~~ three flash floods (Lekach and Schick, 1982). This concentration is very high relative to averages recorded in large perennial rivers such as the tropical Amazon (0.19 grams per liter), Mississippi (0.82 grams per liter) (Milliman and Farnsworth, 2013), or pre-Aswan Nile River (3.43 grams per liter) (Shalash, 1982).

1.4 Recent GAE Flood Research

Eilat, a coastal city established in 1951 with a~~n~~ increasing population of ~~more~~ greater than ~~50~~55,000 people (population 50,000 reported in by Azaryahu, 2005; and 55,000 reported in www.worldpopulationreview.com, accessed in 2025) is located in the northernmost part of the GAE immediately west of the neighboring city of Aqaba, Jordan which is home to over 150,000 residents (Arieli, 2021). Both Eilat and Aqaba expand significantly (> one million visitors) during holiday seasons with tourists arriving to enjoy attractions like the world's northernmost tropical coral reefs (Loya, 2004; Xilotl Soberon And Rofe 2017).

Floods in the GAE can form within hours after rainfall affects the Kinnet watershed in the northern GAE (**Fig. 1**). The Kinnet Canal **(Fig. 2)** serves as a conduit for the Kinnet watershed, channeling both water and sediment loads (predominantly in suspension) toward the lowest elevation point. When the arriving water volume from the catchment area is substantial enough, floods can make their way into the sea (Katz et al., 2015b).
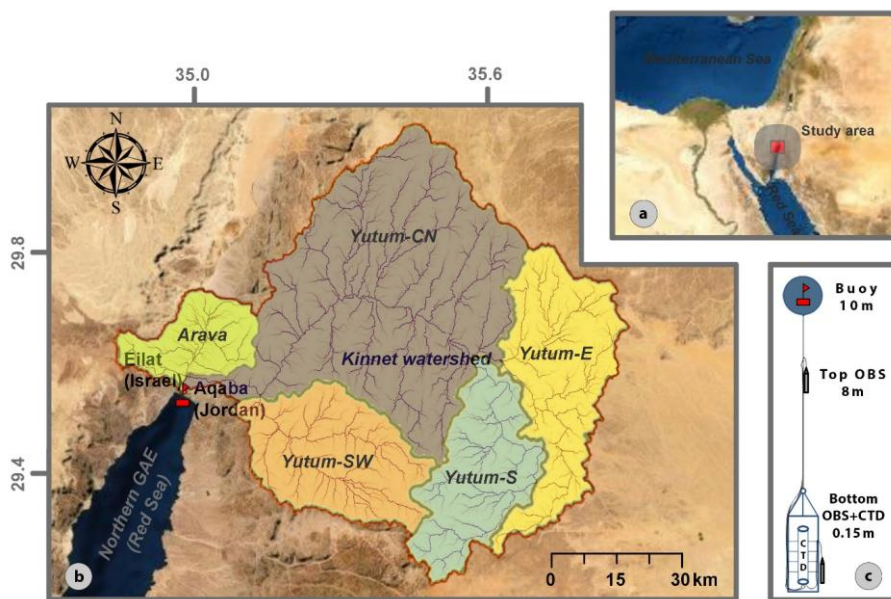
Fig. 1. a) Regional map showing the location of the head of the GAE. (b) Local map illustrates the mooring's position along with ephemeral river systems. The delineation of streams transporting water and sediment to the northern shelf of the GAE is represented by the brown lines. Although all runoff ultimately converges at a single outlet, the Kinnet Canal, dividing the watershed into subbasins helps to identify distinct source areas and improves the estimation of flood arrival at the river mouth (Eilat city center). ~~All ephemeral rivers from Eilat and Aqaba converge into a singular channel, known as the Kinnet Canal, which predominantly serves as a conduit for runoff pathways leading to the sea.~~ Maps adapted from Kalman et al., 2020 (c) Schematic drawing of the

206   mooring station setup (Sea Bird Electric CTD and Campbell Electric 3+ OBS sensors), positioned 250 m
207   offshore the Kinnet outlet at 13 m water depth.
208

209   Flash floods reaching the sea through the Kinnet Canal (discharge located on Eilat shoreline)

210   have been documented since 1994 (Kalman et al., 2020b). Between 1994 and 2012, events

211   were dominated by small to mid-scale floods, intermixed with extended dry periods (Kalman

212   et al., 2020b; Katz et al., 2015b). In 2006, Aqaba was struck by an exceptionally large flood,

213   causing extensive damage (Farhan and Anbar 2014). Historical records also describe

214   significant weather events, including a "terrific rain and hail storm that literally washed away

215   half of modern Aqaba in 1940", and a storm on 11 March 1966, classified as a 50-year return

216   period event (Farhan and Anbar, 2014).

217   The west (Eilat) and the east (Aqaba) sides of the head of the Gulf have different flood

218   potentials. The Wadi Yutum catchment on the east is 4867 km^2, nine times larger than the

219   Arava catchment on the west, and its higher elevation (~1600 m) increases water flow speed

220   and sediment transport. The northern part of Wadi Yutum catchment possesses several sinks

221   and sabkhas in the north, but rainstorms in the rocky southern slopes send water towards

222   Aqaba and the GAE (Farhan and Anaba, 2016). The smaller Arava catchment (458 km^2 and

223   lower elevation (~500 m) still generate floods during rainstorms in the nearby Eilat

224   Mountains.

225   In the northern GAE, Katz et al. (2015) documented a hyperpycnal plume created by a

226   flashflood's high-density sediment load discharging into the sea. Their study characterized the

227   floodwaters (temperature, salinity, sediment concentration) along the coastline and within the

228   plume as well as the sediments deposited on the seafloor. They identified the distribution and

229   thickness of the flood sediments and estimate the volume discharged (approximately 20,000

230   tons), concluding that floods are the most dominant source of GAE seafloor sedimentation.

231   Subsequent investigations explored bioturbation (Mathalon et al., 2019), Late-Holocene

232   climate reconstructions (Kalman et al., 2020b), and anthropogenically-driven changes in

233   sediment dynamics (Kalman et al., 2022).

234

235

2   Data and Methodology

Throughout the study, meteorological data and weather reports surrounding the GAE were closely monitored in order to be 'at ready' in the case of an opportunity to analyze an arriving flash flood. Given that the likelihood of floods occurring in a given day in the year is less than 0.5% (Kalman et al., 2020b), it was unknown whether any floods would actually occur during the designated observational period. Moreover, because of this low likelihood, it was understood that there was a high likelihood that the study could entirely miss an opportunity to make direct measurements, observations, and collections. To counter this issue, the study combined the use of a mooring station that collected regular interval measurements *in situ*, and a multi-person field team, equipped at all times with a field sampling set ready for arriving for taking field measurements if a flash flood occurred (**Fig. 2**). After (if) a flood occurred, the meteorological conditions preceding the production of the flash flood were analyzed in higher resolution. The following describes the methodological sequence performed from the identification of a potential flood event to field measurements, offshore deeper measurement casts, retrieval of mooring array data, and higher resolution meteorological analysis.

Fig. 2. Flash flood entering the northern Red Sea following a heavy precipitation event on 28 October, 2016. Photo by Gal Eyal.

2.1 Meteorological data

~~For t~~The synoptic analysis ~~conducted within the context of~~in this study, used to track
precipitation centers, was based on two data sources. One of these on a regional scale was the
Precipitation Estimation from Remotely Sensed Information using Artificial Neural Networks
(PERSIANN) dataset (Nguyen et al., 2019), obtained via CHRS Data portal, with a 0.5° x
0.5° resolution. Additionally, in a local scale, NASA's Global Precipitation Measurement
(GPM) Integrated Multi Satellite Retrievals (IMERG) with a 0.1° x 0.1° resolution, were
utilized to compensate for the lack of dense meteorological network in the trans-national
Kinnet watershed, located at the northernmost tip of the Gulf of Eilat-Aqaba. Given the
region's hyperarid conditions and limited gauging systems, satellite-derived precipitation data
were essential for accurately estimating precipitated water.

~~images were sourced from the NCEP/NCAR reanalysis dataset, characterized by a 2.5 degree~~
~~x 2.5 degree resolution (Kalnay et al., 1996), and obtained via the NOAA. The necessity to~~

276 The GPM's IMERG data is pivotal in this research due to its advanced capabilities in
277 providing high-resolution precipitation estimates, which are particularly crucial in regions
278 where conventional meteorological infrastructure is sparse or non-existent. The GPM
279 constellation and ground validation suite employ a host of sensors including the active Dual-
280 frequency Precipitation Radar enabling precise measurements of rain rates (Masaki et al.,
281 2014) and the passive GPM Microwave Imager essential for measuring precipitation intensity
282 and distribution (Draper et al., 2015). Following data collection, a series of steps, including
283 ground validation (Tapiador et al., 2020), are undertaken to ensure the accuracy and reliability
284 of the precipitation estimates (Huffman et al., 2020). The subsequent merging of data from
285 various sources, complemented by rigorous quality control and validation procedures
286 culminates in the final IMERG datasets (Huffman et al., 2020).

287 In the specific case of the Kinnet watershed, the utilization of IMERG datasets is
288 indispensableare necessary, and used alone, because physical meteorological stations are
289 sparce. The two stations (Eilat, Israel and Aqaba, Jordan) present in the watershed are only 10
290 kilometers from one another, and show nearly identical annual average precipitation values
291 (*Jordan Meteorological Department, Israel Meteorological Service*, Katz et al., 2015). The

> **Formatted:** Font: Italic

292 absence of adequate ground-based meteorological stations and gauging systems in this
293 hyperarid region makes satellite-derived data the most reliable source for the accurate
294 assessment of precipitation patternsTherefore, they are not useful for measuring the overall
295 contribution of rainfall for the entire watershed. This absence of adequate ground-based
296 meteorological stations and gauging systems in this hyperarid region makes satellite-derived
297 data the most reliable source for the accurate assessment of precipitation patterns. The
298 integration of this high-resolution, satellite-based data with the NCEP/NCAR reanalysis
299 imagery offers a comprehensive understanding of the hydrological dynamics within this trans-
300 national watershed., thus playing a crucial role in the advancement of regional hydrological
301 studies and water resource management.

2.2 *Time series mooring station*

An instrumented mooring station was anchored ~250 m offshore in front of the Kinnet Canal at a depth of 13 m. The instruments on the mooring array included a Sea Bird Electronics SBE 19plus v2 CTD (temperature, salinity, depth) positioned 0.15 m above the seafloor, and three Campbell Electric OBS 3+ optical backscatter sensors calibrated with pure, local flood sediments collected from slackwater deposit near the outlet, and attached to the instrument line at three different depths (0.15m, 2m, 8m) above the seafloor 250 m offshore. Calculations for sediment concentration based on turbidity values from the OBS 3+ sensors was calculated using values derived from direct calibration of sediments from this site (see Mathalon et al. 2019 methods and description). The mooring station instruments collected the properties of the water column for a period of 9 months between April, 2016 and January, 2017. In moored mode, data was collected with a temporal frequency of 300 seconds with 4 measurements per sample. During the mooring period, instruments were cleaned and examined roughly every 10 days by scuba divers, data was retrieved, and the batteries were recharged.

318 ### *2.42.3 Canal measurements*

319 The research team collected a series of measurements and samples from the Kinnet Canal

320 outlet during active flooding (e.g. October 28, 2016 event). Flow speed (m s^{-1}) was calculated

321 based on the surface speed obtained from time a drifting object traveled a predetermined

322 distance (30 meter), corrected (multiplied) by 0.6 to account for riverbed friction due to

323 roughness and riverbed geometry at the measured sequence of the flood (Chie, 1992). Water

324 samples were collected every ~ three hours from the centerline of the waterflow to calculate

325 sediment concentration (g l^{-1}). Similarly, at regular intervals the flood level at the banks was

326 recorded and after the flood had finished, the cross-section areas of the Canal (m^2) for each 3-

327 hour interval were calculated **(Supplementary fig. 1)**.

328

329 ### *2.52.4 Suspended alluvium major element analysis*

330 Major elements (Fe, Al, Mn) were measured from the canal flood water collections. To do

331 this, approximately two grams of dried (60 °C) sediment per sample was ground and

332 homogenized with a mortar and pestle to a powder and analyzed in a vacuum chamber using

333 an ED-XRF (Spectro Scout). The measurements were calibrated with 3-8 certified sediment

334 standards as described in Zirks et al., (2021).

335

336 ### *2.62.5 Stream order and watershed delineation*

337 Hydrological modeling of the Kinnet watershed was performed 1) to understand the time lag

338 between the cessation of rain and initiation of flooding at the river outlet; and 2) to describe

339 hydrological behavior and structure of river system in case of flood events. Digital elevation

340 models (SRTMDEMs) from the Shuttle Radar Topography Mission (SRTM) were

341 downloaded (https://earthexplorer.usgs.gov/) and processed in a series of steps (fill, flow

342 direction, flow accumulation, basin, stream order) using the Hydrology tool (Bajjali, 2017) in

343 ArcGIS Pro (v3.1). This step delineates streams that possess significantly higher potential for

344 flood related hazards.

345

346

347

43 Results

During the study period, a major flash flood event that reached the sea was observed in the last week of October 2016. The results below are presented as a sequence of the event that includes 1) the analysis of mesoscale convective systems during this period, leading to 2) a heavy rainfall and 3) flash flood development with 4) high quantities of transported material in the southern Negev Desert that eventually 5) discharged from the Kinnet Canal to the tip of the northern Gulf of Aqaba-Eilat, Red Sea. The meteorological antecedent conditions leading up to the event were then assessed to consider possible unique features associated with flood production on a regional scale.

4.13.1 Kinnet Catchments

The hydrological analysis of the landscape shows that the Kinnet watershed is the largest among sub-catchments that direct water and sediment into the head of the northern GAE. Modeling performed by incorporating DEM data from satellite imagery delineated two major watershed basins; west (Arava catchment) and east (Yutum catchment) from the pull-apart basin (Wadi Arava) in between. The Yutum catchment is larger in size and, based on topography, can be further subdivided into four sub-basins, contributing uniquely to the overall hydrological dynamics of the hyperarid watershed (Fig 1).

4.23.2 Meteorological Antecedent conditions (Sept 20 – Oct 27)

The initial northward propagation of the Sudan Monsoon Low over the Red Sea (also known as the 'Red Sea Trough', RST) towards the Eastern Mediterranean had begunwas first detected 37 days before heavy precipitation event that formed and eventuallyultimately led to a relatively big large flash flood event in Eilat. Rather than representing a continuous synoptic feature, this period comprised a series of RST-related disturbances with a trough axis retaining in the region and intermittently re-intensifying. Because of thatParticularly, the RST was rather a retained formation of the inverted V shape low tongue, although it strengthened on the 24th, (3 mb over 9 mb), 3 days prior to the massive rainfall (**Supplementary fig. 12**). Congested clouds developed above Ethiopia beginning on Oct 5, but there was no significant formation of clouds until Oct 24th above and in the vicinity of the Red Sea.

On the 24thth, various atmospheric conditions prevailed in the Middle East. At first, velocities of the Polar Front decreased significantly. Based on 200 hPa vector wind map of

380 the day, no sign of a continuous Polar Jet in the region prevailed whatsoever. Satellite

381 imagery shows however a narrow, but long – stretching cloud formation around 22-23°N

382 across the Red Sea and the Arabian Peninsula, in addition to scattered congested clouds above

383 the Southern Red Sea. The 200 hPa vector wind composite confirms that the clouds were

384 formed as a result of enhanced velocities of the STJ (**Supplementary fig. 23**). On Oct 18th,

385 STJ velocities varied between 25-30 ms^{-1}, located at the border of Chad-Lybia-Egypt-Sudan

386 through the Red Sea towards the Middle East. Its shape elongated in east-west direction and

387 its velocity intensified up to 43 ms^{-1} by the 22nd, became the strongest at the difluence over

388 the northern tip of the Persian Gulf. Later, the position of the STJ gradually moved southward

389 and reached its southernmost position on Oct. 27 above the Red Sea at 15-16°N, before

390 moving back northward after the storm.

391   At low atmospheric levels, warm advection that had been formed previously above

392 Sudan and Ethiopia prevailed, resulting in a six-degree temperature rise to 33°C in the center

393 of the Red Sea Trough. Simultaneously, a -9°C and 35% relative humidity (5°C less and 20 %

394 more humid than ambient) upper-level trough reached the Middle East from northwestern

395 direction.

396   These differential warming and cooling effects enhanced static instability with respect

397 to normal conditions. The majority of the moisture (RH=80-90%) to the EM was transported

398 at 700 hPa from tropical Sudan and Ethiopia. During the transport, relative humidity

399 continuously increased in the Levant with no significant change of the temperature profile,

400 which resulted in lowering of the lifting condensation level, embedding to a deep convection

401 above the entire region. Clouds were forming along the fringing mountains at the southern

402 part of the Red Sea on the 25th, but no precipitation occurred.

403

404 *4.33.3 Mesoscale convection*

405 While the RST was approaching the Middle East from the south at low (near sea) atmospheric

406 levels, the well-developed upper-level trough (atmospheric Rossby wave), pointing

407 southwest, formed over the Eastern Mediterranean. As a result, a cold convection took place

408 on the 25th that turned to advection leading to a formation of a cold front over the EM. The

409 combination of lower-level convergence and upper-level divergence are fundamentally linked

410 to enhanced potential for the initiation of intense, but spatially spotty rainstorms due to the

411 topographic heterogeneity of its mountainous local desert environment (El-Fandy, 1950). At

412 the tip of the cold front, advection lifted the airmass above the border of Libya and Egypt and

increased the relative humidity from 30% to 65% at 850 hPa geopotential height (gph). The wind vectors at 700 hPa gph showed that in addition to this humid air was transported towards the Red Sea, the intensified STJ prevailed and effected NE movement of airmasses located in lower atmospheric levels (**Supplementary fig. 3~~4~~**). On the 26th,12.00 pm, congested clouds were formed above the mid-Red Sea and heavy rainfall began ~1000 km south from Eilat (**Supplementary fig. 4~~5~~**).

During the morning of Oct 26, a cloud system of approximately 480 km in diameter was formed above Sinai-southeast Jordan and northwest Saudi Arabia axis. The cloud system developed at the contact zone of the west side of the east pointing RST and the east side of the upper-level trough that occupied the EM at higher atmospheric levels. The rain cells were formed over the ridges along the leeside of the Red Sea mountains, moved further to the middle of the sea, then drifted northward by the RST. Within 18 hours at 0600 UTC 27 October 2016, showers and rainstorms were registered from the entire Negev desert (*Israel Meteorological Service*).

The tip of the RST on the 27th of October reached Cyprus and Syria, its deepest penetration into the Eastern Mediterranean portion of the Middle East. Polar Jet velocities at ~31N latitudes gradually increased, and on this day showed its strongest phase (45 m s^{-1} in the center) and turned 45 degrees, already pointing northeast, reconnecting the opened high-altitude wind system.

The center of the upper-level trough moved from the Nile delta to mid-Egypt within two days (27 Oct), narrowing the contact zone of four (upper-level trough, Red Sea Trough, Polar Jet, and Subtropical Jet) mesoscale systems to approximately 200 km wide channel in the Eastern Mediterranean (**Fig. 3**). As a result, precipitation centers reached the north of the Eastern Mediterranean, but also penetrated further into continental Syria and Iraq. A section of the cold upper-level trough disconnected from the main body of the trough on the 27th, creating a giant 'cold ball' like feature above Eilat, which accelerated its mixing with the near sea level spreaded and warm RST. The northeast-pointing Polar Jet carried and dissipated the trough away and by the end of the day on 28 October, the pressure differences between the atmospheric layers equalized, resulting in the end of the storm.

443
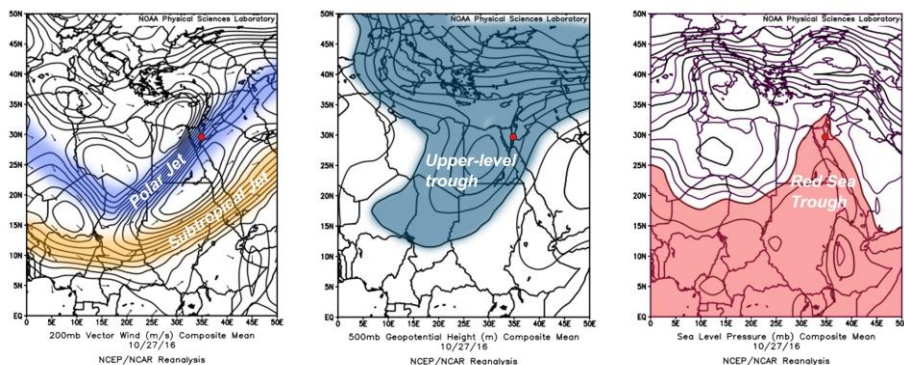
Fig. 3: Composites on the heavy rainfall in Eilat (red dot) showing ~~fo~~threeur mesoscale systems (Polar Jet,
Subtropical Jet, upper-level trough~~, Red Sea Trough~~) and a synoptic scale system (Red Sea Trough) ~~systems~~ in
which their fourfold contact zone narrowed down to ~200 km wide gap over the Eastern Mediterranean
contributing to the formation of the historical flashflood.

4.43.4 Precipitation and Flashflood entering the sea

A flash flood reached the head of the GAE at ~3:00 am October 28th, 2016; after an Active

RST accompanied by scattered showers and thunderstorms made contact with a high-pressure

belt over the mid-latitudes and inundated the Middle East region from Egypt, through Israel,

Jordan, as well as Lebanon and Syria. The RST moved from the mid to the northern Red Sea

within 18 hours. During this time, nearly every segment of the 4867 km^2 Kinnet watershed

received some amount of precipitation (**Fig. 4**), which eventually contributed to the formation

of a flash flood. The total precipitated rain during this time was calculated at 133 million m^3

in the Kinnet catchment, accumulating for ~51 hours prior to the flashflood's arrival into the

GAE.
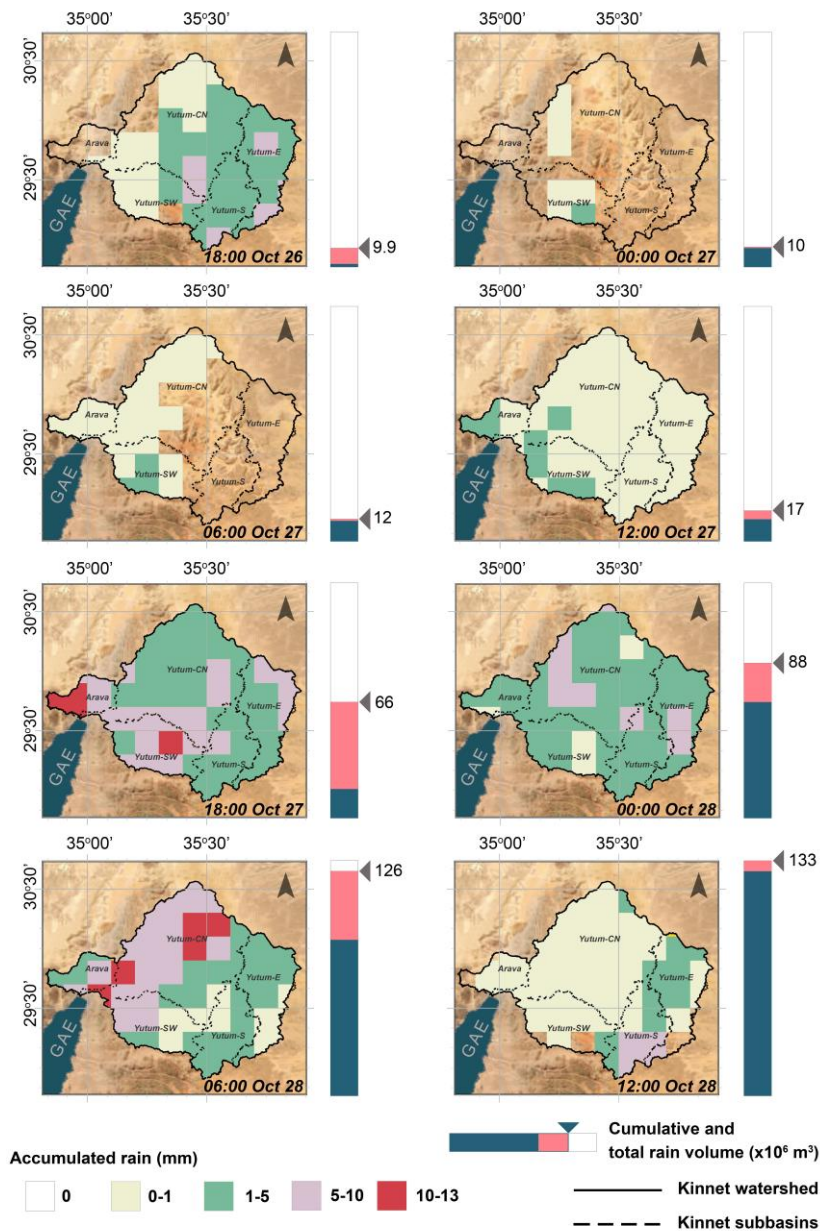
459
460
461 **Fig. 4:** GPM-IMERG satellite precipitation showing 6h rain development in the Kinnet watershed in 0.1°
462 x0.1°resolution. Accumulated rain during hours between measurements (red bar) and total accumulated rain
463 volume (blue +red bars) indicate that the majority of the water precipitated within only 18 hours.

464

During the precipitation period, rain was temporally and spatially unevenly distributed. For
the first 24 hours, scattered and localized rain events in the catchment area resulted in the
arrival of a total of 17 million m^3 water (~13 % of the total). In the following 18 hours
however, both sides of the Arava Valley (Eilat and Wadi Yutum catchments) experienced
intense storms, adding 109 million m^3 water (~82% of the total). The last 6 hours resulted in
an accumulation of an additional 7 million m^3 rain water (~5% of the total), but similarly to
the initial phase of the event, it was spatially spotty and mostly precipitated in the eastern side
(Yutum-S, Yutum-SE) of the watershed. It was followed by a 6-hour no precipitation period,
before precipitating only ~52.000 m^3 rain (0.04%) at both spatially and temporally highly
varied stages.

     According to conversations with witnesses, some flood waters arrived at the head of
the GAE after the middle of the night, around 3 AM on the 28th of October (see **Fig. 5**), but no
turbid water, only elevated discharge was described. The research team performed the first
recording and sampling at 9AM and continued to take 8 measurements for 30 hours.
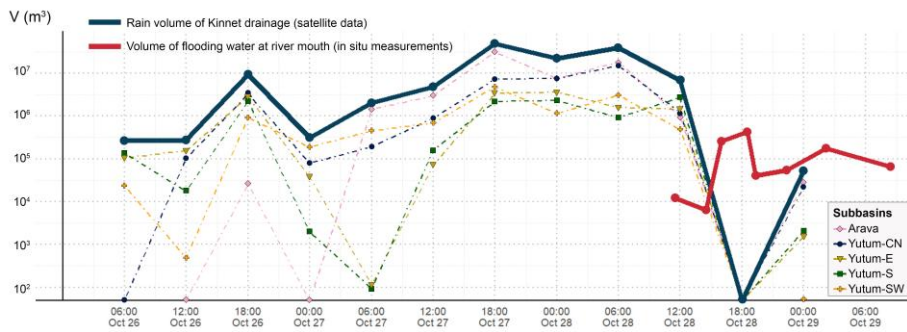
Fig. 5. Summary of quantitative analysis of the water before and during flooding on the 28th of October, 2016 in
Eilat based on satellite data and in-situ measurements. The distribution of the rain amongst the subbasins (dashed
lines) indicate the patchy nature (unevenly distributed) of rain events in this hyperarid environment at the first 36
hours of the storm, which was followed by concentrated and elevated quantities of rainfall in all subbasins.
According to witnesses, the flash flood arrived at the sea at 9 o'clock in the morning and transported large
quantities of suspended sediment over a period of 30 hours.

491

492 The water flow and the sediment concentrations of the flood increased from 1.33 m^3 s^{-1} and

493 20.73 g l^{-1} at 9 AM to 47.42 m^3 s^{-1} and 20.91 g l^{-1} at 2:30 PM, respectively. By 6:30 PM the

494 flow decreased to 13.53 m^3 s^{-1} and the sediment concentration increased to 27.55 g l^{-1} and by

495 2:30 AM in the next day the flow was further reduced to 2.87 m^3 s^{-1} and the sediment

496 concentrations rose to a 33.5 g l^{-1}. In total, 1.04 * 10^6 m^3 water flowed into the sea through the

497 Kinnet Canal and transported 2.44 *10^4 tons of sediment over approximately 30 hours, which

498 the majority of this quantity was then deposited on the shallow marine shelf. The sea surface

499 discoloration from transported sediments was visible for as long as 7 days. Estimations

500 extrapolated from the elemental analysis of the samples taken during the event suggest that

501 1014 tons of Fe, 1413 tons of Al, and 20 tons of Mn entered the sea.

502 Indications of the arriving flood waters were also recorded by the offshore mooring

503 station instruments (**Fig. 6**). According to the sensors, water temperature did not change, but

504 water salinity and turbidity started to fluctuate at 9:50 AM on the 28th of October, 2016, 250

505 m offshore the canal outlet. They These two parameters followed an opposite trend and

506 changed periodically but periodic changes at the initial stage of the flood mirrored one another,

507 as salinity dropped turbidity rose and vice versa. Ten minutes after midnight, turbidity

508 increased to as high as 2.18 g l^{-1} sediment concentration, and salinity near the seafloor

509 dropped to 38.73 PSU, a value that is 1.80 PSU less than the mean salinity (40.53 PSU)

510 recorded over the 9 months of observations from this site. During the last stage of the flood,

511 salinity returned to just below-background values 6 hours after its lowest measured value

512 (~40.4 PSU), while turbidity was still highly variable. Later, this variance with minimal

513 amplitudes was limited only to the bottommost conditions and remained diversified hours

514 after the cessation of the flood.

515

516

517
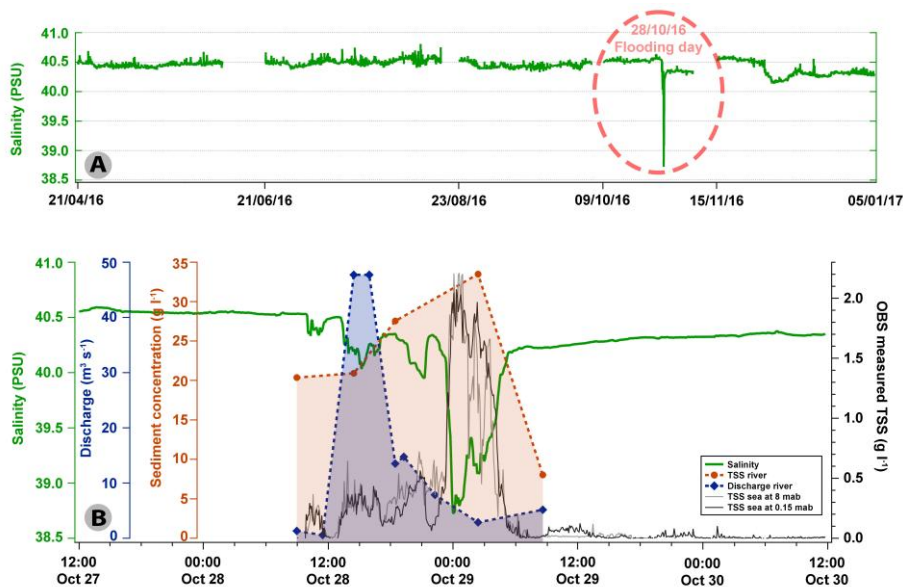
518 **Fig. 6.** Offshore mooring array measurements (A and B) and Kinnet water and sediment discharge collection and

519 recording results including the flood event of October 28, 2016. A) Nine months of salinity measurements from

520 the mooring station. The flooding event is clearly visible as a sudden decrease in salinity. No significant

521 temperature change was registered during the event. Gaps in the data indicate the periods during which the

522 instruments were removed for downloading data and maintenance. B) On-land measurements of changing of the

523 flood discharge and sediment concentration over time, and expanded view of three days of mooring station

524 measurements (TSS and salinity) including immediately before and after the flooding event. The OBS turbidity

525 sensors from the 3 m depth (top) and 0.15 m depth ('bottom') both show fluctuations and increases coinciding

526 with the arrival of flood water.

527

54 Discussion

This study followed the sequence of a storm that occurred on 28 October, 2016 in Eilat from its initial phase to and through a flash flood that started deposited alluvium in the northern Red Sea a day later. The flood was the 13th flood recorded since records began in 1994 (Katz et al., 2015; Kalman et al., 2020). From 1994 to 2012, there was a drought period wherein flood occurrence was below one per year (0.17), followed by increased occurrence of 1.7 floods per year (2012-2020). With regard to the hazard level of the 28 October 2016 flood event, no death occurred, nor was property damage reported; and transportation and infrastructure (roads and airport) were not affected. The interpretation of reanalysis data revealed that multiple unstable atmospheric conditions led to the formation of the storm that within a day exceeded the annual average precipitation in Eilat. It began with the northern propagation of the RST three days prior to actual flash floods forming in the southern Negev. Tropical moisture was transported towards the Red Sea and enhanced velocities of the Polar Jet and intensified RST expansion towards the Eastern Mediterranean. At the same time, a well-developed upper-level cold front approached the Eastern Mediterranean and the combination of lower-level convergence and upper-level divergence initiated an intense rain event associated with thunderstorms.

5.14.1 Storm analysis and implications

At sea level, the RST as one of the key elements in the formation of the storms is one of the main synoptic patterns that influence weather in the Levant region (Alpert et al., 2004b). The northward propagation of this low-pressure system is not a rare case; RST is formed 43.7% of the days between October and November during the rainy season (Saaroni et al., 2020). This means that RST is present roughly every second day during these months, providing the potential for heavy precipitation to form. Saaroni et al. (2020) developed an algorithm that identifies the northern part of the RST and classifies it according to the location of the trough axis with respect to longitude 35ºE. This classification is important because RST expansion and orientation influences the distribution of a possible storm over the Levant in its "active" (ARST) phase (Kahana et al., 2002).

Hochman et al, (2021) used CMIP5 climate projections to categorize winter RSTs and analyzed their characteristics and impacts on the region. They found that rainfall associated with wet RST (WRST) is projected to decline by 37% by the end of the 21st century due to shifts in atmospheric circulation patterns, increased temperatures, and a reduction in the

561 frequency and intensity of WRST events. Additionally, they found that extreme precipitation
562 events related to the WRST show distinct atmospheric pattern differences when compared to
563 lighter precipitation events within the same system (Hochman et al., 2023).
564   Ziv et al., (2005) showed a December 1993 ARST example with flooding wherein a
565 persistent southerly flow from over the Red Sea prior to the event (in addition to tropical
566 moisture transport) induced air ascendance along the Red Sea, and carried it to the
567 surrounding regions. During the October 2016 case, however, two days prior to the flood, at
568 the tip of the upper-level trough, advection lifted the airmasses above the border of Libya and
569 Egypt (westward of the study area) and increased the relative humidity by 35%, which was
570 then transported towards the Red Sea. Such elevated air moisture values fit those used in
571 Krichak et al., (2012)'s algorithm for identifying ARST events. They concluded that high
572 moisture content in the air influences the intensity of the developing storm in the Eastern
573 Mediterranean; and conversely, drier air masses along the Eastern Mediterranean coasts
574 reduces the possibility (and intensity) for an ARST event. The conditions observed during this
575 2016 event support the presence of an ARST event. In some rare cases, the lowest flank of the
576 upper-level trough can disconnect from the meandering mid-latitude upper-level low system;
577 and can form into an individual cut-off low resulting in a negative upper-level temperature
578 anomaly. This is extremely favorable for thunderstorms in the atmosphere and can lead to and
579 induce fatal flashfloods on land (Dayan et al., 2021).
580   At upper atmospheric levels, major mid - and high latitude cyclonic and anti-cyclonic
581 systems affect the atmospheric Rossby waves (e.g. extension, direction and persistent time of
582 upper-level troughs and ridges), and it is the cold upper-level trough introduced from northern
583 regions that enhanced convective instability during the October event. A negative phase of the
584 North Atlantic Oscillation created an amplified Rossby wave three days prior to the flood,
585 resulting in two upper-level troughs extending southward: one in the Western Mediterranean
586 up to latitude 17 degrees and one in the Eastern Mediterranean up to latitude 15 degrees.
587 Because of a weak polar vortex, the cold air from the arctic region (from Scandinavia in the
588 case of the eastern type) could escape, creating a hole in the Ferrel cell that cut through the
589 Polar Front, and triggered the ARST event (**Video-1**). Since the polar vortex began to
590 strengthen again on the 25th, enhanced velocities of the Polar Front "arrived" to the EM, and
591 in the absence of the Polar Front, ran into the Subtropical Jet stream. By the following day,
592 the enhanced high altitude wind pushed STJ at least 2 degrees further south, meanwhile Polar
593 Jet winds bounced back from this mid-latitude waveguide (Branstator, 2002) and further
594 enhanced its velocities in the following days. Similar conditions were described in southwest

595 Asia by Saligheh, (2021); and concluded that pulling the Polar Jet southward that merges into

596 the Subtropical Jet stream can enhance cyclogenesis and lead to hydrodynamic instability.

597 Asiri et al., (2020); studied specifically the STJ over Africa and the Middle East and found

598 based on nearly 60 years of reanalysis data that its north-south shifting is controlled by the

599 temporal extension of the Azores High and the Siberian High. When the Azores High is

600 weakened or shrank westward, the STJ shifts southward; and when the Siberian High is

601 weakened or shrank eastward, the STJ shifts northward. This is in agreement with the October

602 2016 event. Prior to the Eilat flooding, the Azores High weakened and the STJ track gradually

603 shifted southward and its position only changed direction when the Azores High was

604 beginning to increase.

605

606 ### 5.24.2 From precipitation to flow into the sea

607 During the October 2016 flooding event, the Kinnet watershed received 133 million m^3 rain

608 although most of the rain precipitated on the Jordanian mountains in the Wadi Yutum

609 catchment (**Fig. 4**). Rainfalls in the desert are typically described as short lived and intense

610 (Sharon, 1972); under extreme conditions they have been recorded as delivering ~110 mm

611 within 3 hours (Youssef et al., 2016). This is certainly true for observations made in singular

612 locations; whereas the satellite measurements show the overall lingering presence of the

613 event.

614   The timing from the onset to final cessation of rainfall (including initial 12 hour

615 minimal precipitation period and a 6-hour gap) was 66 hours. During that time, floods were

616 produced within the wadis in the watershed. Rain cells above the Kinnet watershed initially

617 developed only in its eastern side, then later on in the entire watershed, and in some cases

618 significantly larger amounts precipitated in the vicinity of Wadi Arava and Yutum-CN

619 subbasin (**Fig.ure 1b**). This flood was most likely facilitated by the first rain period that pre-

620 soaked the ground (13% of the total precipitation), but it is likely the second rainy spell that

621 provided the runoff that ultimately ended in the discharged flood water as the majority of the

622 rain precipitated within the following 18 hours (82% of the total precipitation).

623

624 After the cessation of the rain, wadis continued to receive runoff which flowed downslope

625 towards the outlet of the Kinnet Canal and the sea. This flow reached the sea approximately

626 50 hours after the rain started, and roughly 3 hours after most of the rainfall ended.

627

Formatted: Font: Bold

Unfortunately, in the poorly monitored (very low spatial dispersion of gages and weather stations) catchment area of the October 2016 event it was not possible to assess the transmission losses of the precipitated water. To overcome this issue and give an estimation of water loss from the formation of the rain until water discharge at the river mouth, we used GPM-IMERG precipitation data that has been shown to correlate well with precipitation gauge data both in humid (Pradhan et al., 2022; Yang et al., 2018) and arid regions (Chen et al., 2020; Mohammed et al., 2020). It is important to note that its $0.1°$ x $0.1°$ (100 km²) spatial resolution (10x10 km grid) does not allow to analyze precipitation accumulated in wadis and lower ranked streams specifically (which is important because same rain event can cause flooding in a particular wadi, while the neighboring wadi remains dry), making the quantification of the patchy nature of a hyperarid rain event impossible; its 30 minute temporal resolution however enables to capture the sum of the precipitated water and give us the confidence to apply its dataset on the nearly 5000 km² Kinnet watershed. We calculate that approximately 133 million m³ precipitated in the entire watershed of the Kinnet Canal during this event and that ~1 million m³ (0.75 %) of it ultimately reached the GAE through the Kinnet Canal. This limited yield reflects the fact that runoff from more distant parts of the watershed (particularly from the eastern sub-basins) faces greater losses due to longer travel distances, allowing for increased infiltration and evaporation. The ~99% difference reflects infiltration relating to a complex matrix of soil properties and variations in rain intensity, duration, location and evaporation. In arid regions where sequential gage sequence measurements were madeconducted, transmission loss rates greatly showed varied from considerable variations. For example, e.g. 13.2 % in an Australian desert stream in Australian (Dunkerley and Brown, 1999) to up to 98% in areas parts ofin Saudi Arabia (Walters, 1990); 20% 85% , and in between 20% and 85%, located in Nahal Zin, in Negev Desert, Israel's Negev Desert (Greenbaum et al., 2001).

GPM data stretches back 21 years and gives us the opportunity to investigate which areas in the watershed have high(er) probabilities for the water to accumulate (**Fig. 7**). The 2000-2021 window in Eilat covers 12 years from a prolonged drought period (1994-2012) characterized by three flashfloods only, and a more humid 8-year period (2012-2020) with the occurrence of 12 flashfloods in total (Kalman et al., 2020b).
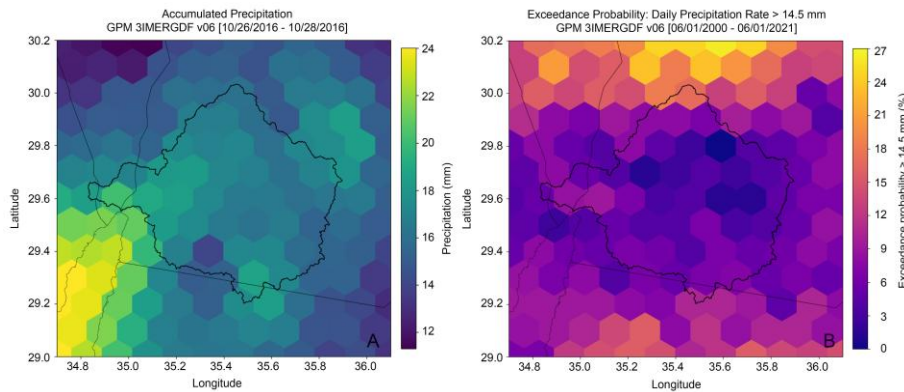
Fig. 7. GPM-IMERG data visualized in the Kinnet watershed at the head of the Gulf of Aqaba-Eilat, Red Sea. A) Sum of accumulated rain preceding a flashflood on 27 October, 2016. B) ~~Sum of accumulated rain preceding a flashflood on 27 October 2016. (B)~~ Likelihood of precipitation exceeding 14.5 mm. This threshold corresponds to a local flashflood event recorded on 1 March 2017, when 14.5 mm of rain fell in under 3 hours and temporarily flooded the streets of Eilat. This threshold was used to assess flashflood potential across the basin. Likelihood values represent the proportion of days with precipitation exceeding 14.5 mm relative to the total number of days during the analyzed period (2000–2021).

~~Likelihood of precipitation exceeding 14.5 mm.~~

Fig.7A shows the sum of precipitated water within the Kinnet watershed that preceded the formation of the Oct 27, 2016 flooding event in Eilat. The main accumulation centers during the event were around the surroundings of Wadi Arava and within the Yutum-center sub-basin. Because of the hypersensitivity for extreme weather events of the region, there is a great variety in the distribution of the rainwater that describe each precipitation event. Therefore, the accumulated precipitation case is rather a description of this particular event than an analog to generalize the distribution of the precipitation during any flashflood events.

On March 1, 2017, a small flashflood was generated after a hailstorm directly affected the Eilat mountains. The accumulated water in Eilat gauge station was 14.5 mm (54% of the yearly total) that precipitated within 3 hours. Streets were flooded and closed quickly, but also were reopened within an hour, because rain water was not sufficient enough to induce waterflow in Yutum ephemeral riverbeds that, if it had occurred, would arrive with a lag to the Kinnet outlet and to its surroundings. Because the rain event was local and could trigger a flashflood, its precipitation (14.5 mm) was used as a threshold value to calculate exceedance probabilities for the Kinnet watershed (**Fig.7B**). The highest probabilities for exceeding the threshold value can be found around the Wadi Arava, the southern Jordanian mountains and

685 the northern part of the Yutum-center subbasin. On the other hand, in the center of the
686 Yutum-center subbasin, the likelihood of exceeding the threshold value is near zero. The
687 southern probabilities may be explained by the orographic effect, which forces the RST to
688 flow over high topography as well as the northern probabilities may be explained by the
689 interannual position of the diffluence of the upper-level trough interacting with the RST, and
690 resulting in explosive cyclogenesis (Kouroutzoglou et al., 2015; Ziv et al., 2022).
691

692 ### 5.34.3 *Sediment dispersal at sea*

693 Based on the flow and sediment concentrations in the Kinnet canal we calculated that during
694 the October 2016 flashflood, approximately 24,000 tons of suspended sediment entered the
695 sea. This value likely and slightly underestimates the true total, as measurements were not
696 available during the initial onset and possibly the waning stage of the flood. Nevertheless, the
697 estimate captures the main body of the event and is representative of the overall magnitude.
698 This The amountvalue is similar to the reported 21,000 tons of suspended sediment
699 transported to the GEA from the Kinnet Canal during the Feb 2013 flash flood event (Katz et
700 al., 2015b). In both cases the amount far exceeded the annual airborne dust introduced into the
701 northern Gulf of Aqaba-Eilat (Chen et al., 2008). From shallow water sediment cores Katz et
702 al. (2015) roughly estimated average of circa 10 kg sediment per meter square coverage of the
703 alluvium on the seafloor primary deposition zone after a historical flooding in February 2006,
704 which magnitude corresponds with 6 kg sediment on average per meter square coverage
705 produced by the October 2016 event.
706 When desert floods arrive into the sea, if their sediment concentrations are high
707 enough, their bulk density becomes higher than that of the seawater and they are expected to
708 produce hyperpycnal flows that plunge and progress along the seafloor as turbidity currents
709 (Katz et al., 2015b). This high sediment load drags fresher water beneath saltier water layers
710 that would otherwise float above the saltier, denser seawater. If however, sediment
711 concentrations are not high enough and the bulk density of the discharged floodwater is lower
712 than that of the seawater, they form hypopycnal plumes that disperse at and near the sea
713 surface. Notably, in some cases hypopycnal flows can generate turbidity currents due to
714 trickling down (fingering) and amassing of suspended sediments near the seafloor (Parsons et
715 al., 2001).
716 According to witnesses, the Eilat flood arrived to the sea at 3 AM on the 28th of
717 October, however the mooring data registered the initiation of salinity decrease and turbidity

718 increase only at 9.50 AM in the morning, ~ 7 hours later. If these reports are correct, then this

719 time lag between visual notice and instrumental registration suggests either low sediment

720 concentrations in the discharged water at this initial stage that caused only a hypopycnal

721 plume or a very slow (~1 cm s^{-1}), offshore progression of the mixed flood water. It was also

722 possible that the witnesses in the darkness observed higher discharge without significantly

723 elevated sediment concentration, which water might have originated from a nearby

724 desalination factory. With no measurements from the station at this time, this question

725 remains open. Flood related turbidity at the measuring station lasted from 9.50 AM Oct 28

726 until 5.15 PM Oct 29 and the increased turbidity was registered at approximately the same

727 time in the 0.15 and 8 mab sensors (**Fig. 6**). This would suggest that by the time floodwater

728 reached the station they were already mixed (though not homogeneously) in the water

729 column. During the ~31 hours of the registered event, salinity and sediment concentrations at

730 the measuring station mirror-imaging one another demonstrating considerable fluctuations

731 near the seafloor (**Fig. 6**). Taking into consideration that there is some lag between the outlet

732 and the measuring station, these fluctuations were likely caused by changes in floodwater and

733 sediment discharge from the Kinnet canal. Such fluctuations would result from changes in the

734 intensity and geographical distribution of the rainfall at the catchment area, many hours

735 earlier. At its peak, salinity at the moored station was reduced to 38.75 ‰ which is

736 approximately 1.75 ‰ less than the measured salinity in the 7 months of measurements prior

737 to the event. This drop is 19 times greater than the standard deviation of the salinity observed

738 during that period. This drop clearly demonstrates that the freshwater arriving with the

739 flashflood was denser due to its high sediment load, and therefore was forced downward

740 rather than being distributed on the water surface. ~~This~~ The drop coincided with the highest

741 TSS to salinity ratios suggesting a concurrent increase in sediment concentrations in the

742 discharged floodwater (**Fig.8a**).

743

744
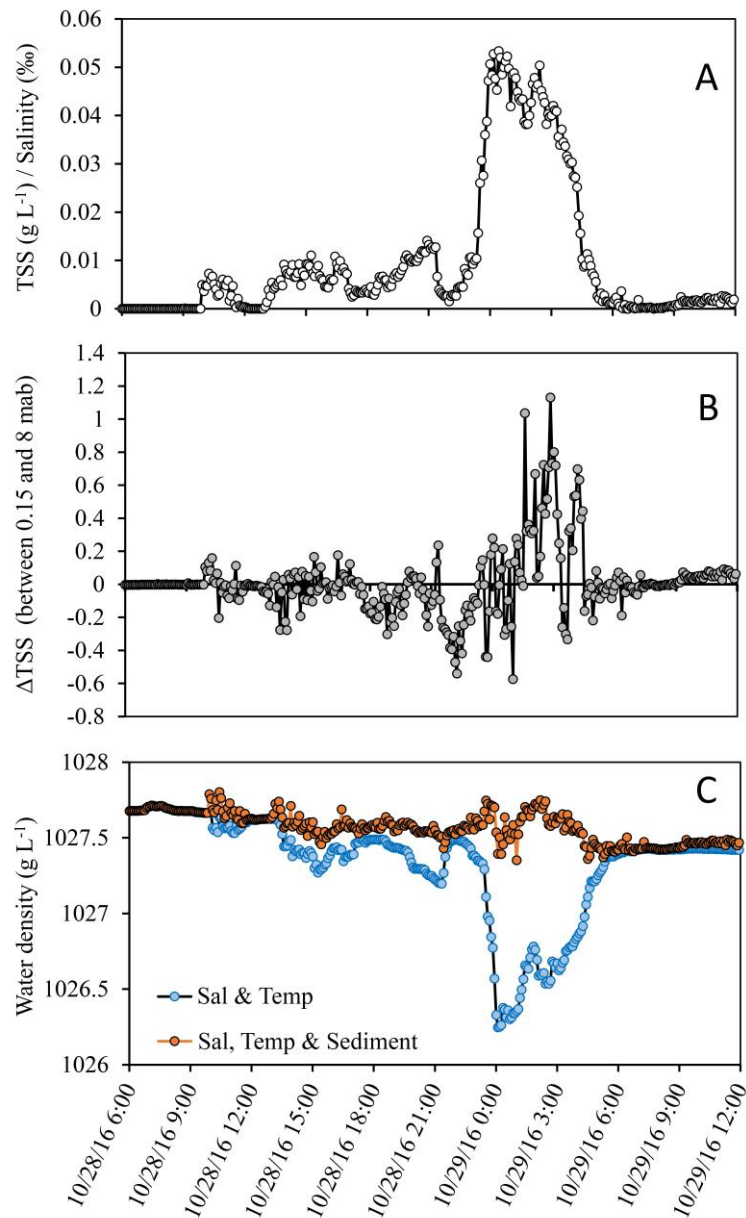
745 **Fig. 8.** Measurements of an offshore mooring station of the Oct 27, 2016 flashflood event that reached the sea in

746 the northern Gulf of Aqaba-Eilat. The floodwater discharged with low salinities loaded with high concentrations

747 of suspended sediments to the sea (A), resulted in both hypo- and hyperpycnal plumes (B), and elevated bottom

748 water densities (C) during the evolution of the flood.

Moreover, during this and three prior, though much smaller events, sediment concentrations near the seafloor (0.15 mab) were higher than those measured at 8 mab, (**Fig.8b**). Although floodwater and sediments were found throughout the water column at the station area early on, these measurements indicate intermittent occurrences of hyperpycnal flows during this time. This assumption is supported by calculated density of the bottom water, based only on the temperature and salinity and then after correcting it with the suspended sediment concentrations (assuming mean sediment particles density of 2.65 g cm^{-3}.). The results, shown in **Fig. 8c** demonstrate that the freshening of the seawater alone would have greatly reduced the bottom water density, causing it to float. However, when corrected with the suspended sediment concentrations, the bulk density of the near bottom water occasionally exceeds that of the undiluted seawater, enabling it to plunge and progress as a hyperpycnal flow. Even more so, when considering the gradual decrease in the salinity (and hence density) of the water column offshore the Kinnet outlet during the flood which further decreased the incoming floodwater buoyancy. Notably, in the 5, discrete measurements of sediment concentrations that were made in the Kinnet Canal during the flood, the highest value was 33.5 g l^{-1}. This value is considerably less than the required ~43 g l^{-1} to cause direct hyperpycnal plumes in the head of the GAE (Katz et al., 2015b). We therefore expect that at the beginning of the floods, convective fingering of sediment from above may have caused smaller hyperpycnal events near the seafloor (Parsons et al., 2001). Conversely, the major hyperpycnal flow that was registered at the marine station between 11:00 pm Oct 28th and 4:30 AM Oct 29th was likely caused by direct plunging of dense flood water. This would suggest that sometime around 2:00 am in the 9 hours between the 3rd and 4th TSS measurements, sediment concentrations in the Kinnet did may have reached the required minimum threshold (36-43 g/l) to generate this a hyperpycnal plume upon entering the GAE. Sediment concentrations measurementsd at the outlet during both the 3rd and 4th collections were around likely declined substantially before reaching the marine station, with observations indicating up to a 15-fold higher relative to the marine station decrease over the 250 m transport distanceoffshore. These values record the process of both dilution with seawater and sediment dispersal as the suspected plume traveled along the seafloor. It is therefore reasonable to assume, given the relatively low sediment concentration values recorded (2.18 g/l) at 250 m offshore that the proposed hyperpycnal plume collapsed before reaching the stationdissipated before reasing the station's sensors. While a hyperpycnal plume may not have been present at that distance, , yet sediment dispersal continued in the form of in

783   ~~the form of weaker~~ near-bottom transport~~.~~, possibly enhanced by added sediment entrained in

784   the turbulent flow~~or settling from a subsiding surface layer. This increase in the sediment~~

785   ~~concentrations onshore was missed because of the long intervals between samplings.~~ Salinity

786   returned to near ~~ambient~~ background levels by 5:45 AM Oct 29, and remained at ~ 40,3 PSU,

787   ~0,2 PSU less than average until the retrieval of the mooring 9 days after the flood event.

788

789

5.44.4 *Storms, Rain, Flashfloods, and Planning*

In this study, we show how climate and sediments are related. The synoptic analysis of the storms illustrate what key parameters contribute to the triggering mechanism of a storm and where in the particular watershed is likely to rain. Using reanalysis data, all these parameters can be collected for each flood event and a database can be formed. When flooding, large quantities of sediments from the catchments can be transported to the sea, where they may serve as a climate archive. Although sediments upon arriving to the sea in the northernmost GAE undergo different levels of post-depositional processes that alter their physical-chemical properties; by recognizing changes in flood deposit signatures, it is possible to reconstruct past climatic variations on the seafloor downcore (Kalman et al., 2020~~b~~, 2022; Katz et al., 2015~~b~~). ~~Similarly to~~Just as atmospheric parameters ~~found~~ are catalogued in synoptic ~~analysis~~analyses, the physical and ~~-~~chemical properties of ~~the~~ flash flood sediments in their deposition~~al areas~~settings can be ~~collected~~ compiled in~~to the same~~the same database, ~~creating atmospheric (~~linking atmospheric trigger~~)~~s with ~~-~~ sedimentary ~~(~~response~~s) pairs for the record~~. While the use of ~~We therefore suggest that these pairs can serve as training examples for~~ machine learning ~~algorithms~~requires large datasets, we propose that in locations where distinct flood layers are consistently preserved (potentially hundreds of well-characterized sediment-climate pairs)~~and hence help to interpret what atmospheric conditions prevailed that contributed to specific sediment patterns in the record before reanalysis data existed~~, such datasets could be developed and applied to train machine learning models. It is expected that the combined analysis of climatology, hydrology and sedimentology of flash flood events will help to better understand the interlinkages between the otherwise separately discussed aspects of flood hazards in hyperarid regions **(Fig. 9)**. Furthermore, it will impose careful site selection and proper planning in the establishment of new coastal cities and already existing cities planning to expand.
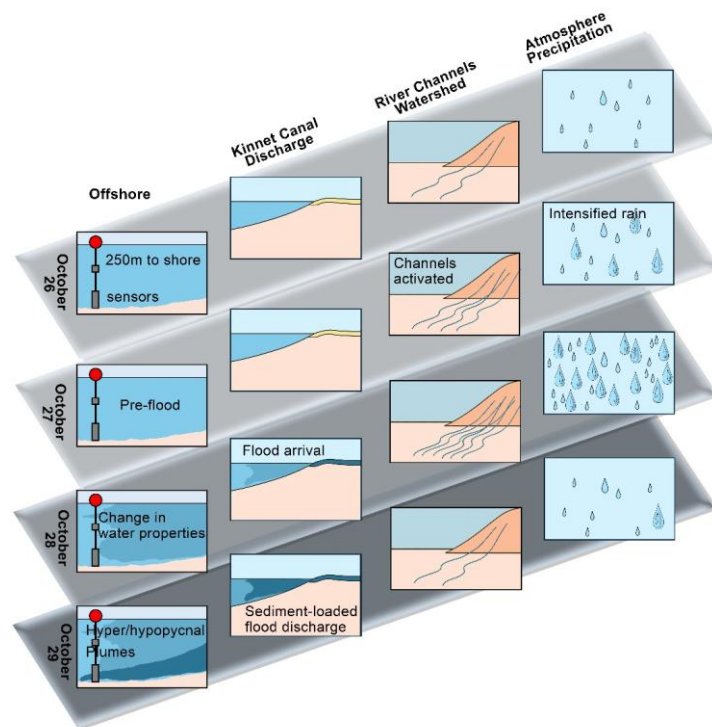
Fig. 9: Sequence of sediment transport processes during the October 2016 flash flood in Eilat. The figure illustrates daily changes from October 26–29, 2016, showing the evolution of sediment transport from precipitation to offshore deposition in the northern Red Sea. It details concurrent developments in offshore waters, at the canal discharge point, within the watershed, and includes rainfall intensity for each day. The seven key stages include: (1) atmospheric conditions conducive to precipitation, (2) precipitation events, (3) watershed drainage, (4) flash flood formation, (5) sediment and water transport to the coastline, (6) discharge at the coastal outlet, and (7) marine dispersal and deposition.

~~6~~5 Conclusions

A hyper arid region flashflood event was studied from its preceding meteorological
conditions, precipitation, run-off development, and ending with its arrival into the Gulf of
Eilat-Aqaba. It was observed that a negative phase of the North Atlantic Oscillation triggered
an amplified Rossby wave, whereas its lower flank reached the Levant region and created
thunderstorms leading to an exceptional 3-day long rain event in Eilat, Israel. The
precipitation was unevenly distributed in the watershed, and needed 51 hours to reach the
Kinnet canal outlet. Only 0.75 % of the precipitated water reached the sea eventually.
Sediment transport into the sea during this single event far exceeded annual airborne dust
precipitation. Both hypo- and hyperpycnal plumes during the flood event were instrumentally
captured. It is concluded that meteorological and climate precursors are the earliest to identify
actual environmental conditions, and since precipitation and sedimentation are linked, flash
flood born sediment in marine deposits can provide a key to identifying paleoclimatic trends
that together can serve as basic input for developing early warning systems against flash
floods and related hazards.

76 Data availability

The data supporting the findings of this study is available from the corresponding author upon reasonable request.

87 Video supplement

The video supplement (Video-1) illustrating the visualization of cold air escaping from the Arctic region and triggering the ARST event is attached to this manuscript as *Video-1-Kalman-et-al.gif*."

98 Author contribution

Conceptualization: AK, TK, PH, BGT

Data curation: AK, TK, MV, JL, BGT

Formal analysis: AK, TK, MV, JL

Investigation: AK, AM

Methodology: AK, TK, AM, PH, BGT

Visualization: AK, TK, MV, JL, BGT

Writing – original draft preparation: AK

Writing – review & editing: AK, TK, MV, JL, AM, PH, BGT

Supervision: TK, BGT

Resources: TK, PH, BGT

Project administration: AK, TK, BGT

Funding acquisition: TK, PH, BGT

109 Competing interests

The authors declare that they have no conflict of interest.

1110 Acknowledgement

The research was funded by the Schulich Foundation Canada-Israel Collaboration Project, the Ministry of Interior, Israel and the Yohay Ben-Nun Foundation NAF-IOLR. The authors thank the Interuniversity Institute for Marine Sciences Eilat for general support and members of the Institute who contributed during *in situ* sampling of the flash flood in harsh and sometimes dangerous conditions. We thank Professor Hadas Saaroni for her thorough and precious feedback. Special thanks to Eyal Amitai, Emanuel Sestieri, Erez Levin, Asher Meir, Ofir Hameiri, Sivan David, Gabriele Guerrini, Gal Eyal, and Guilhem Banc-Prandi.

12**11** **References**

Allison, M. A., Demas, C. R., Ebersole, B. A., Kleiss, B. A., Little, C. D., Meselhe, E. A., Powell, N. J., Pratt, T. C., and Vosburg, B. M.: A water and sediment budget for the lower Mississippi–Atchafalaya River in flood years 2008–2010: Implications for sediment discharge to the oceans and coastal restoration in Louisiana, J. Hydrol., 432–433, 84–97, https://doi.org/https://doi.org/10.1016/j.jhydrol.2012.02.020, 2012.

Alpert, P., Osetinsky, I., Ziv, B., and Shafir, H. (2004a): Semi-objective classification for daily synoptic systems: Application to the eastern Mediterranean climate change, Int. J. Climatol., 24, 1001–1011, https://doi.org/10.1002/joc.1036., 2004.

Alpert, P., Osetinsky, I., Ziv, B. and Shafir, H. (2004b), A new seasons definition based on classified daily synoptic systems: an example for the eastern Mediterranean. Int. J. Climatol., 24: 1013-1021. https://doi.org/10.1002/joc.1037,

Arieli, T.: Aqaba and Eilat: Twenty-five years of 'good neighborly relations' in a post-conflict environment, in: Twin Cities across Five Continents, Routledge, 133–146, 2021.

Ashbel, D.: Great floods in Sinai Peninsula, Palestine, Syria and the Syrian Desert, and the influence of the red sea on their formation, Q. J. R. Meteorol. Soc., 64, 635–639, https://doi.org/https://doi.org/10.1002/qj.49706427716, 1938.

Asiri, M. A., Almazroui, M., and Awad, A. M.: Synoptic features associated with the winter variability of the subtropical jet stream over Africa and the Middle East, Meteorol. Atmos. Phys., 132, 819–831, 2020.

Awad, A.M. and Almazroui, M., 2016. Climatology of the winter Red Sea trough. Atmospheric Research, 182, pp.20-29, https://doi.org/10.1016/j.atmosres.2016.07.019

Azaryahu, M.: The beach at the end of the world: Eilat in Israeli popular culture, Soc. Cult. Geogr., 6, 117–133, https://doi.org/10.1080/1464936052000335008, 2005.

Bajjali, W.: ArcGIS for environmental and water issues, Springer, 2017.

912

Barragán, J. M. and de Andrés, M.: Analysis and trends of the world's coastal cities and agglomerations, Ocean Coast. Manag., 114, 11–20, https://doi.org/10.1016/j.ocecoaman.2015.06.004, 2015.

Blum, M. D. and Törnqvist, T. E.: Fluvial responses to climate and sea-level change: a review and look forward, Sedimentology, 47, 2–48, https://doi.org/https://doi.org/10.1046/j.1365-3091.2000.00008.x, 2000.

Branstator, G.: Circumglobal teleconnections, the jet stream waveguide, and the North Atlantic Oscillation, J. Clim., 15, 1893–1910, 2002.

Chen, C., Chen, Q., Qin, B., Zhao, S., and Duan, Z.: Comparison of different methods for spatial downscaling of GPM IMERG V06B satellite precipitation product over a typical arid to semi-arid area, Front. Earth Sci., 8, 536337, 2020.

Chen, Y., Paytan, A., Chase, Z., Measures, C., Beck, A. J., Sañudo-Wilhelmy, S. A., and Post, A. F.: Sources and fluxes of atmospheric trace elements to the Gulf of Aqaba, Red Sea, J. Geophys. Res. Atmos., 113, 1–13, https://doi.org/10.1029/2007JD009110, 2008.

Chie, Y. Ben: Dimensionally Homogeneous Manning's Formula, J. Hydraul. Eng., 118, 1326–1332, https://doi.org/10.1061/(ASCE)0733-9429(1992)118:9(1326), 1992.

Clapp, E. M., Bierman, P. R., Schick, A. P., Lekach, J., Enzel, Y., and Caffee, M.: Sediment yield exceeds sediment production in arid region drainage basins, Geology, 28, 995–998, https://doi.org/10.1130/0091-7613(2000)28<995:SYESPI>2.0.CO;2, 2000.

Cohen, H. and Laronne, J. B.: High rates of sediment transport by flashfloods in the Southern Judean Desert, Israel, Hydrol. Process., 19, 1687–1702, https://doi.org/10.1002/hyp.5630, 2005a.

Cohen, H. and Laronne, J. B.: High rates of sediment transport by flashfloods in the Southern Judean Desert, Israel, Hydrol. Process., 19, 1687–1702, https://doi.org/10.1002/hyp.5630, 2005b.

946 Cools, J., Vanderkimpen, P., El Afandi, G., Abdelkhalek, A., Fockedey, S., El Sammany, M.,
947 Abdallah, G., El Bihery, M., Bauwens, W., and Huygens, M.: An early warning system for
948 flash floods in hyper-arid Egypt, Nat. Hazards Earth Syst. Sci., 12, 443–457, 2012.
949

950 Dayan, U., Ziv, B., Margalit, A., Morin, E. Y., and Sharon, D.: A severe autumn storm over
951 the middle-east : synoptic and mesoscale convection analysis, 122, 103–122,
952 https://doi.org/10.1007/s007040170038, 2001.
953

954 Dayan, U., Ziv, B., Shoob, T., and Enzel, Y.: Suspended dust over southeastern
955 Mediterranean and its relation to atmospheric circulations, Int. J. Climatol., 28, 915–924,
956 https://doi.org/https://doi.org/10.1002/joc.1587, 2008.
957

958 Dayan, U., Lensky, I. M., Ziv, B., and Khain, P.: Atmospheric conditions leading to an
959 exceptional fatal flash flood in the Negev Desert, Israel, Nat. Hazards Earth Syst. Sci., 21,
960 1583–1597, https://doi.org/10.5194/nhess-21-1583-2021, 2021.
961

962 Draper, D. W., Newell, D. A., Wentz, F. J., Krimchansky, S., and Skofronick-Jackson, G. M.:
963 The global precipitation measurement (GPM) microwave imager (GMI): Instrument overview
964 and early on-orbit performance, IEEE J. Sel. Top. Appl. Earth Obs. Remote Sens., 8, 3452–
965 3462, 2015.
966

967 Dunkerley, D. and Brown, K.: Flow behaviour, suspended sediment transport and
968 transmission losses in a small (sub-bank-full) flow event in an Australian desert stream,
969 Hydrol. Process., 13, 1577–1588, 1999.
970

971 El-Fandy, M.G., 1948. The effect of the sudan monsoon low on the development of thundery
972 conditions in Egpyt, Palestine and Syria. Quarterly Journal of the Royal Meteorological
973 Society, 74(319), pp.31-38.
974

975 El-Fandy, M. G.: Effects of Topography and Other Factors on the Movement of Lows in the
976 Middle East and Sudan, Bull. Am. Meteorol. Soc., 31, 375–381, https://doi.org/10.1175/1520-
977 0477-31.10.375, 1950.
978

979 Farhan, Y. and Anaba, O.: Flash Flood Risk Estimation of Wadi Yutum (Southern Jordan)

Watershed Using GIS Based Morphometric Analysis and Remote Sensing Techniques, Open J. Mod. Hydrol., 06, 79–100, https://doi.org/10.4236/ojmh.2016.62008, 2016.

Farhan, Y. and Anbar, A.: Fragile Landscape: Impact and Consequences of May 2014 Flash-flood Disaster in the Aqaba Area, Southern Jordan, Res. J. Environ. Earth Sci., 6, 451–465, https://doi.org/10.19026/rjees.6.5257, 2014.

Gee, G. W. and Hillel, D.: Groundwater recharge in arid regions: Review and critique of estimation methods, Hydrol. Process., 2, 255–266, https://doi.org/https://doi.org/10.1002/hyp.3360020306, 1988.

Greenbaum, N., Enzel, Y., and Schick, A. P.: Magnitude and frequency of paleofloods and historical floods in the Arava basin, Negev Desert, Israel, Isr. J. Earth Sci., 50, 159–186, https://doi.org/10.1092/N5VU-FU5F-QNWC-UDCK, 2001.

Haggag, M. and El-Badry, H.: Mesoscale Numerical Study of Quasi-Stationary Convective System over Jeddah in November 2009, Atmos. Clim. Sci., 03, 73–86, https://doi.org/10.4236/acs.2013.31010, 2013.

Hereford, R., Webb, R. H., and Longpré, C. I.: Precipitation history and ecosystem response to multidecadal precipitation variability in the Mojave Desert region, 1893-2001, J. Arid Environ., 67, 13–34, https://doi.org/10.1016/j.jaridenv.2006.09.019, 2006.

Hickey, B. M., Kudela, R. M., Nash, J. D., Bruland, K. W., Peterson, W. T., MacCready, P., Lessard, E. J., Jay, D. A., Banas, N. S., Baptista, A. M., Dever, E. P., Kosro, P. M., Kilcher, L. K., Horner-Devine, A. R., Zaron, E. D., McCabe, R. M., Peterson, J. O., Orton, P. M., Pan, J., and Lohan, M. C.: River Influences on Shelf Ecosystems: Introduction and synthesis, J. Geophys. Res. Ocean., 115, https://doi.org/https://doi.org/10.1029/2009JC005452, 2010.

Hochman, A., Alpert, P., Kunin, P., Rostkier-Edelstein, D., Harpaz, T., Saaroni, H., and Messori, G.: The dynamics of cyclones in the twentyfirst century: the Eastern Mediterranean as an example, Clim. Dyn., 54, 561–574, https://doi.org/10.1007/s00382-019-05017-3, 2020.

Hochman, A., Rostkier-Edelstein, D., Kunin, P. et al. Changes in the characteristics of 'wet' and 'dry' Red Sea Trough over the Eastern Mediterranean in CMIP5 climate projections. Theor Appl Climatol 143, 781–794 (2021).

Hochman, A, Plotnik, T, Marra, F, Shehter, E-R, Raveh-Rubin, S & Magaritz-Ronen, L 2023, 'The sources of extreme precipitation predictability; the case of the 'Wet' Red Sea Trough', *Weather and Climate Extremes*, vol. 40, 100564. https://doi.org/10.1016/j.wace.2023.100564

Holdren, J. P. and Ehrlich, P. R.: Human population and the global environment, Am. Sci., 62, 282–292, 1974.

Huffman, G. J., Bolvin, D. T., Braithwaite, D., Hsu, K.-L., Joyce, R. J., Kidd, C., Nelkin, E. J., Sorooshian, S., Stocker, E. F., and Tan, J.: Integrated multi-satellite retrievals for the global precipitation measurement (GPM) mission (IMERG), Satell. Precip. Meas. Vol. 1, 343–353, 2020.

Kahana, R., Ziv, B., Enzel, Y., and Dayan, U.: Synoptic climatology of major floods in the Negev Desert, Israel, Int. J. Climatol., 22, 867–882, https://doi.org/10.1002/joc.766, 2002.

Kalman, A., Katz, T., Hill, P., and Goodman-Tchernov, B.: Droughts in the desert: Medieval Warm Period associated with coarse sediment layers in the Gulf of Aqaba-Eilat, Red Sea, Sedimentology, 67, 3152–3166, https://doi.org/10.1111/sed.12737, 2020a.

Kalman, A., Katz, T., Hill, P., and Goodman-Tchernov, B.: Droughts in the desert: Medieval Warm Period associated with coarse sediment layers in the Gulf of Aqaba-Eilat, Red Sea, Sedimentology, n/a, https://doi.org/10.1111/sed.12737, 2020b.

Kalman, A., Goodman-Tchernov, B., Hill, P., Everhardt IV, C., Mathalon, A., and Katz, T.: Anthropogenic changes in waterways produce "drought-like" layers in shelf sediments, Elem. Sci. Anthr., 10, 39, https://doi.org/10.1525/elementa.2021.00039, 2022.

Kalnay, E., Kanamitsu, M., Kistler, R., Collins, W., Deaven, D., Gandin, L., Iredell, M., Saha, S., White, G., Woollen, J., Zhu, Y., Chelliah, M., Ebisuzaki, W., Higgins, W., Janowiak, J., Mo, K. C., Ropelewski, C., Wang, J., Leetmaa, A., Reynolds, R., Jenne, R., and Joseph, D.: The NCEP/NCAR 40-Year Reanalysis Project, Bull. Am. Meteorol. Soc., 77, 437–472,

https://doi.org/10.1175/1520-0477(1996)077<0437:TNYRP>2.0.CO;2, 1996.

Katz, T., Ginat, H., Eyal, G., Steiner, Z., Braun, Y., Shalev, S., and Goodman-Tchernov, B. N.: Desert flash floods form hyperpycnal flows in the coral-rich Gulf of Aqaba, Red Sea, Earth Planet. Sci. Lett., 417, 87–98, https://doi.org/10.1016/j.epsl.2015.02.025, 2015a.

Katz, T., Ginat, H., Eyal, G., Steiner, Z., Braun, Y., Shalev, S., and Goodman-Tchernov, B. N.: Desert flash floods form hyperpycnal flows in the coral-rich Gulf of Aqaba, Red Sea, Earth Planet. Sci. Lett., 417, 87–98, https://doi.org/10.1016/j.epsl.2015.02.025, 2015b.

Kouroutzoglou, J., Flocas, H. A., Hatzaki, M., Keay, K., Simmonds, I., and Mavroudis, A.: On the dynamics of a case study of explosive cyclogenesis in the Mediterranean, Meteorol. Atmos. Phys., 127, 49–73, 2015.

Krichak, S. O. and Alpert, P.: Role of large scale moist dynamics in November 1-5, 1994, hazardous Mediterranean weather, J. Geophys. Res. Atmos., 103, 19453–19468, https://doi.org/10.1029/98JD01710, 1998.

Krichak, S. O., Breitgand, J. S., and Feldstein, S. B.: A conceptual model for the identification of active Red Sea trough synoptic events over the southeastern Mediterranean, J. Appl. Meteorol. Climatol., 51, 962–971, 2012.

Lekach, J. and Schick, P.: Suspended sediment in desert floods in small catchments, Isr. J. Earth-Sciences, 31, 144–156, 1982.

Loya, Y.: The coral reefs of Eilat—past, present and future: three decades of coral community structure studies, in: Coral health and disease, Springer, 1–34, 2004.

Masaki, T., Kubota, T., Oki, R., Kojima, M., Furukawa, K., Miura, T., Kai, H., Iguchi, T., Hanado, H., and Yoshida, N.: Development of level 1 algorithm of dual frequency precipitation radar (DPR) for the global precipitation measurement (GPM), in: 2014 IEEE Geoscience and Remote Sensing Symposium, 4962–4965, 2014.

Mathalon, A., Goodman-Tchernov, B., Hill, P., Kálmán, Á., and Katz, T.: Factors influencing

flashflood deposit preservation in shallow marine sediments of a hyperarid environment, Mar. Geol., 411, 22–35, https://doi.org/10.1016/j.margeo.2019.01.010, 2019.

Merz, B., Blöschl, G., Vorogushyn, S., Dottori, F., Aerts, J. C. J. H., Bates, P., Bertola, M., Kemter, M., Kreibich, H., Lall, U., and Macdonald, E.: Causes, impacts and patterns of disastrous river floods, Nat. Rev. Earth Environ., 2, 592–609, https://doi.org/10.1038/s43017-021-00195-3, 2021.

Milliman, J. D. and Farnsworth, K. L.: River discharge to the coastal ocean: a global synthesis, Cambridge University Press, 2013.

Mohammed, S. A., Hamouda, M. A., Mahmoud, M. T., and Mohamed, M. M.: Performance of GPM-IMERG precipitation products under diverse topographical features and multiple-intensity rainfall in an arid region, Hydrol. Earth Syst. Sci. Discuss., 2020, 1–27, 2020.

Mulder, T., Syvitski, J. P. M., Migeon, S., Faugères, J. C., and Savoye, B.: Marine hyperpycnal flows: Initiation, behaviorand related deposits. A review, Mar. Pet. Geol., 20, 861–882, https://doi.org/10.1016/j.marpetgeo.2003.01.003, 2003.

Mullenbach, B. L. and Nittrouer, C. A.: Rapid deposition of fluvial sediment in the Eel Canyon, northern California, Cont. Shelf Res., 20, 2191–2212, https://doi.org/https://doi.org/10.1016/S0278-4343(00)00067-4, 2000.

Neumann, B., Vafeidis, A. T., Zimmermann, J., and Nicholls, R. J.: Future coastal population growth and exposure to sea-level rise and coastal flooding - A global assessment, PLoS One, 10, https://doi.org/10.1371/journal.pone.0118571, 2015.

Nguyen, P., Shearer, E., Ombadi, M., Gorooh, V., Hsu, K., Sorooshian, S., Logan, W. and Ralph, M. (2020). PERSIANN Dynamic Infrared–Rain Rate Model (PDIR) for High-Resolution, Real-Time Satellite Precipitation Estimation. *Bulletin of the American Meteorological Society* 101(3) pp. E286-E302. Available at: https://journals.ametsoc.org/view/journals/bams/101/3/bams-d-19-0118.1.xml.

Parsons, J. D., Bush, J. W. M., and Syvitski, J. P. M.: Hyperpycnal plume formation from

1116   riverine outflows with small sediment concentrations, Sedimentology, 48, 465–478, 2001.

1117

1118   Pradhan, R. K., Markonis, Y., Godoy, M. R. V., Villalba-Pradas, A., Andreadis, K. M.,

1119   Nikolopoulos, E. I., Papalexiou, S. M., Rahim, A., Tapiador, F. J., and Hanel, M.: Review of

1120   GPM IMERG performance: A global perspective, Remote Sens. Environ., 268, 112754, 2022.

1121

1122   Reid, I. and Frostick, L. E.: Flow dynamics and suspended sediment properties in arid zone

1123   flash floods, Hydrol. Process., 1, 239–253,

1124   https://doi.org/https://doi.org/10.1002/hyp.3360010303, 1987.

1125

1126

1127   Saaroni, H., Harpaz, T., Alpert, P., and Ziv, B.: Automatic identification and classification of

1128   the northern part of the Red Sea trough and its application for climatological analysis, Int. J.

1129   Climatol., 40, 3607–3622, https://doi.org/10.1002/joc.6416, 2020.

1130

1131   Saligheh, M.: The Effect of Merging Subtropical Jet Stream and Polar Fronts Jet Stream on

1132   Heavy Rainfall in Southwest Asia, 2021.

1133

1134   Schick, A. P. and Lekach, J.: A~~N EVALUATION~~n evaulation ~~OF~~ of ~~TWO~~ two ~~TEN-~~

1135   ~~YEAR~~ten-year ~~SEDIMENT BUDGETS~~sediment budgets, ~~NAHAL~~ Nahal ~~YAEL~~Yael,

1136   ~~ISRAEL~~Israel, Phys. Geogr., 14, 225–238, https://doi.org/10.1080/02723646.1993.10642477,

1137   1993.

1138

1139   Shalash, S.: Effects of sedimentation on the storage capacity of the High Aswan Dam

1140   reservoir, Hydrobiologia, 91–92, 623–639, https://doi.org/10.1007/BF00000061, 1982.

1141

1142   Sharon, D.: The spottiness of rainfall in a desert area, J. Hydrol., 17, 161–175,

1143   https://doi.org/https://doi.org/10.1016/0022-1694(72)90002-9, 1972.

1144

1145   Shentsis, I., Meirovich, L., Ben-Zvi, A., and Rosenthal, E.: Assessment of transmission losses

1146   and groundwater recharge from runoff events in watercourses of the Neqarot watershed,

1147   Israel, Isr. J. Earth Sci., 50, 201–215, https://doi.org/10.1092/J79L-39QP-NC9G-WFTF,

1148   2001.

1149

Small, C. and Nicholls, R.: A Global Analysis of Human Settlement in Coastal Zones, J. Coast. Res., 19, https://doi.org/10.2307/4299200, 2003.

Syvitski, J. P. M., Vörösmarty, C. J., Kettner, A. J., and Green, P.: Impact of humans on the flux of terrestrial sediment to the global coastal ocean, Science (80-.)., 308, 376–380, https://doi.org/10.1126/science.1109454, 2005.

Tapiador, F. J., Navarro, A., García-Ortega, E., Merino, A., Sánchez, J. L., Marcos, C., and Kummerow, C.: The contribution of rain gauges in the calibration of the IMERG product: Results from the first validation over Spain, J. Hydrometeorol., 21, 161–182, 2020.

Tsvieli, Y. and Zangvil, A.: Synoptic climatological analysis of "wet" and "dry" Red Sea Troughs over Israel, Int. J. Climatol., 25, 1997–2015, https://doi.org/10.1002/joc.1232, 2005.

de Vries, A. J., Ouwersloot, H. G., Feldstein, S. B., Riemer, M., El Kenawy, A. M., McCabe, M. F., and Lelieveld, J.: Identification of Tropical-Extratropical Interactions and Extreme Precipitation Events in the Middle East Based On Potential Vorticity and Moisture Transport, J. Geophys. Res. Atmos., 123, 861–881, https://doi.org/10.1002/2017JD027587, 2018.

De Vries, A. J., Tyrlis, E., Edry, D., Krichak, S. O., Steil, B., and Lelieveld, J.: Extreme precipitation events in the Middle East: Dynamics of the Active Red Sea Trough, J. Geophys. Res. Atmos., 118, 7087–7108, https://doi.org/10.1002/jgrd.50569, 2013.

Walters, M. O.: Transmission losses in arid region, J. Hydraul. Eng., 116, 129–138, 1990.

Yang, H. F., Yang, S. L., Xu, K. H., Milliman, J. D., Wang, H., Yang, Z., Chen, Z., and Zhang, C. Y.: Human impacts on sediment in the Yangtze River: A review and new perspectives, Glob. Planet. Change, 162, 8–17, https://doi.org/10.1016/j.gloplacha.2018.01.001, 2018.

Youssef, A. M., Sefry, S. A., Pradhan, B., and Alfadail, E. A.: Analysis on causes of flash flood in Jeddah city (Kingdom of Saudi Arabia) of 2009 and 2011 using multi-sensor remote sensing data and GIS, Geomatics, Nat. Hazards Risk, 7, 1018–1042, https://doi.org/10.1080/19475705.2015.1012750, 2016.

1184 Zirks, E., Krom, M., Schmiedl, G., Katz, T., Xiong, Y., Alcott, L. J., Poulton, S. W., and
1185 Goodman-Tchernov, B.: Redox evolution and the development of oxygen minimum zones in
1186 the Eastern Mediterranean Levantine basin during the early Holocene, Geochim. Cosmochim.
1187 Acta, 297, 82–100, https://doi.org/10.1016/j.gca.2021.01.009, 2021.

1188

1189 Ziv, B., Dayan, U., and Sharon, D.: A mid-winter, tropical extreme flood-producing storm in
1190 southern Israel: Synoptic scale analysis, Meteorol. Atmos. Phys., 88, 53–63,
1191 https://doi.org/10.1007/s00703-003-0054-7, 2005.

1192

1193 Ziv, B., Harpaz, T., Saaroni, H., and Blender, R.: A new methodology for identifying
1194 daughter cyclogenesis: Application for the Mediterranean Basin, Int. J. Climatol., 35, 3847–
1195 3861, https://doi.org/10.1002/joc.4250, 2015.

1196

1197 Ziv, B., Shimer, R., Harpaz, T., Drori, R., Alpert, P., Raveh-Rubin, S., and Saaroni, H.:
1198 Identification and classification of the wet Red Sea Trough over Israel, Int. J. Climatol., 42,
1199 10062–10082, https://doi.org/10.1002/joc.7884, 2022.

1200

1201